(Received 21 February 2025, Accepted 1 April 2025, Scheduled 4 April 2025)

Temperature Dependent Design of Streamlined Ablatable Radomes for Hypersonic Applications

Rudra N. Barik, Aparna Parameswaran, and Hrishikesh S. Sonalikar*

Department of Electrical & Electronics Engineering, BITS Pilani, Goa Campus, India

ABSTRACT: This paper presents the temperature-dependent design of streamlined constant and variable thickness ablatable radomes for hypersonic applications. An optimized three-layer radome wall configuration is proposed, consisting of a radome shell sandwiched between an outer ablative layer and an inner matching layer. The outer ablative layer offers protection against temperatures up to 1600°F, while the inner matching layer effectively prevents total internal reflections. The radome shell is designed using an inhomogeneous planar layer model to account for the temperature gradient existing across its thickness. The numerical analysis of the radome wall is done using the 3D ray tracing method with aperture integration. Power transmission and boresight error characteristics of the radomes remain stable over a thermal operating range of 250°F to 1600°F. The performance of the radomes in dynamic flight conditions is analyzed using the time step analysis. Post ablation, the power transmission of constant thickness and variable thickness radomes remains well above −0.6 dB and −0.5 dB, respectively. The broadband performance of both radomes is analyzed over the X-band. Except for the boresight direction, the power transmission over the X-band remains above −1 dB for all incidence angles. The maximum boresight error is observed to be less than 4.29 mrad over the X-band.

1. INTRODUCTION

The problem of extreme heating of streamlined radomes used in space exploratory vehicles and hypersonic airborne applications due to intense aerodynamic friction is of great importance in aerospace research [1, 2]. An antenna enclosed by a hot radome will experience significant performance degradation, affecting the quality of the transmitted or received electromagnetic (EM) signals [3]. Therefore, the radomes used in hypersonic applications must be protected from extreme heat [4]. This may be accomplished by using a coating of ablative material on the surface of the radome [5]. An ablative material is a heat shield that protects the radome by absorbing and dissipating the heat influx, thus preventing excessive heating of the radome [6, 7]. The ablative materials are classified into melting ablators [8] and charring ablators [9]. The ablative layer, as well as the process of ablation, can influence the performance of the enclosed antenna. The extent of this influence can be analyzed by studying the radome power transmission (PT) and boresight error (BSE) characteristics during the ablation taking place in a dynamic hypersonic environment [10].

In [11], the performance of an enclosed antenna and electronic components was analyzed during the ablation of a streamlined monolithic radome. A compensation method based on the coupled electro-mechanical model of the system was proposed to minimize the performance degradation of the radar guidance system caused by ablation. Following this, a volume integral equation-based algorithm was presented to compute the BSE and boresight error slope (BSES) of a monolithic radome in [12]. In this work, the variations in permittivity and radome profile due to the ablation of the radome tip region were considered while predicting radome performance parameters. A study on multi-layered variable thickness ceramic radome for hypersonic applications was presented in [13]. This study examined how variations in thermal conductivity affect radome performance parameters in a steady-state temperature field. Also, the asymmetric insertion phase delay distribution was quantitatively related to the radome BSE. Recently, the effect of laminar ablation on the radome installed on the reentry vehicle was presented in [14], and the degradation in PT and BSE was computed using the finite integral time domain method. Although the simulations performed in these works are pretty comprehensive, the possibility of using an additional ablatable layer to protect the radome shell was not explored.

In [15], a radome with a hybrid cone-tangent geometry was analyzed. The radome wall had a fiberglass core layer and an ablative Duroid or Avcoat coating. Different combinations of materials and thicknesses were studied to seek the optimum two-layered radome wall, producing the minimum distortion on the sum pattern of the antenna. This work used fixed values of electrical parameters for the materials. As a result, the effects of temperature on radome performance were not considered. Following this, a concept of an adaptively ablatable radome was published in [16]. In this patent, the protection of the conical radome shell at high temperatures was proposed using an outer ablatable layer. The optimization of ablative layer thickness to compensate for the thermal expansion of the radome shell was also proposed. In [17] and [18], a planar radome covered with an outer ablative layer was analyzed and designed using an inhomogeneous planar layer (IPL) model by considering

* Corresponding author: Hrishikesh Shashikant Sonalikar (p20220012@goa.bits-pilani.ac.in).

the temperature gradient spanning across the radome wall. Recently, an inhomogeneous radome wall with an outer thermal protection layer was analyzed in [1], considering the effects of temperature on material properties, changes in thickness due to ablation, and thermal expansion. In these works, although a better power transmission was achieved at elevated temperatures using the IPL model, the power transmission at higher angles of incidence was limited due to reflections occurring at the interface of the radome shell layer and outer ablative layer. Realizing this, a three-layer planar radome wall configuration with layers of the same ablative material on both sides of the radome shell was proposed in [19] to achieve improved performance at higher angles of incidence.

Based on this literature review, it can be concluded that only a few works are available on the design and analysis of streamlined radomes with the protection of ablative layers. Therefore, in this paper, we have taken up the design of streamlined constant and variable thickness radomes with ablative layers. The novelty of the work can be summarized as follows:

- Use of the optimized three-layer wall configuration with outer ablative layer and inner matching layer avoids total internal reflection and provides good PT performance of greater than -0.02 dB.
- A comprehensive analysis of ray transmission and aperture phase distribution is carried out to justify the inclusion of a matching inner layer in the radome wall configuration.
- The designed radomes maintain stable performance in the thermal operating range of 250°F to 1600°F. The maximum co-pol PT of constant and variable thickness radomes is -0.1 dB and -0.029 dB, respectively.
- Both designed radomes exhibit stable performance despite variations in the thickness of the outer ablative layer. Even post ablation, the PT for the constant and variable thickness radomes remains above -0.6 dB and -0.5 dB, respectively.
- Due to the three-layer wall configuration, the proposed radomes exhibit broadband performance over the X-band (8 GHz–12 GHz), maintaining PT above -1 dB and maximum BSE of 4.29 mrad.

The structure of the paper is as follows. Section 2 describes the modeling of the antenna-radome system. Section 3 is about the design and analysis of ablatable radomes. Section 4 highlights the performance of the proposed radomes in dynamic flight conditions, while Section 5 describes the effect of ablation on the radome performance. In Section 6, the performance of the radomes over a broadband frequency range is analyzed. Section 7 compares the performance of the proposed radomes with the existing literature. Finally, Section 8 concludes the paper with remarks.

2. MODELING OF ANTENNA-RADOME SYSTEM

2.1. Antenna-Radome System

In Fig. 1, the radome geometry enclosing a 10 GHz array antenna is presented. The radome has a tangent-ogive profile with

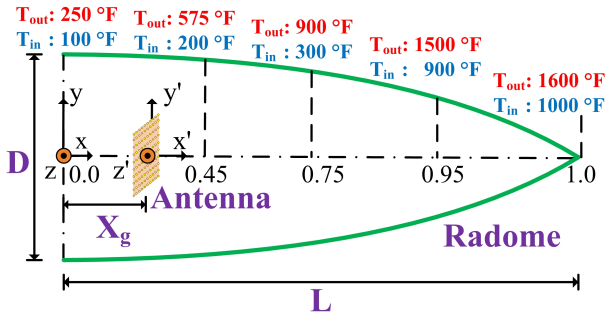

FIGURE 1. Antenna-radome configuration with temperature distribution data points. (x', y', z') is the antenna coordinate system and (x, y, z) is the radome coordinate system. x-y is the elevation plane and x-z is the azimuth plane. T_{out} and T_{in} represent the temperatures at the outer and the inner surfaces of the radome wall, respectively.

an aspect ratio of 2 : 1, where the length (L) is 1 m, and the diameter (D) is 0.5 m. An array of 10×10 source points with 0.5λ spacing between them constitutes the antenna aperture. The antenna is positioned 0.3 m from the radome base. The radiated fields are vertically polarized (y'). The temperature distribution on the outer and inner surfaces of the radome wall corresponding to distinct positions on the radome axis is represented by T_{out} and T_{in} respectively. It is observed that the inner temperature increases from 100°F at the base to 1000°F at the tip of the radome. Similarly, the outer surface temperature increases from 250°F at the base to 1600°F at the tip of the radome wall.

2.2. Radome Wall Configuration

A radome operating in a hypersonic environment needs protection from adverse temperature effects. This may be accomplished by providing an outer coating of a suitable ablative material. As the ablative layer usually has a dielectric constant lower than that of the radome shell, reflections occur at the interface between the radome shell and ablative layer at higher angles of incidence. This limits the power transmission capability of the antenna. Therefore, an additional coating of the same ablative material is provided on the inner surface of the radome shell. The result is a B-sandwich radome wall configuration that maintains the incidence angle below the critical angle at the interface between the radome shell and outer ablative layer, thereby avoiding unnecessary reflections. Hence, the proposed radome wall configuration comprises an inner layer, a radome shell, and an outer ablative layer, as shown in Fig. 2.

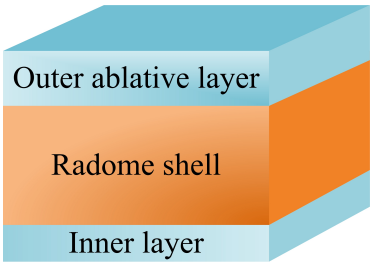

FIGURE 2. The proposed radome wall configuration.

The material chosen for the radome shell is Pyroceram 9606 ($\epsilon_r = 5.515$, $\tan\delta = 0.0003$) due to its excellent properties at high temperatures [20]. The inner layer and outer ablative layer are composed of Teflon ($\epsilon_r = 2.001$, $\tan\delta = 0.0001$) [21]. Here, the dielectric constant and loss tangent are given for ambient temperature. Being a non-charring ablative material, Teflon is desirable for applications where radio frequency (RF) signals are transmitted or received through the radome [5].

2.3. The Inhomogeneous Planar Layer Model

In hypersonic applications, a streamlined radome develops a spatial temperature distribution on both the outer and inner surfaces. Table 1 presents a typical spatial temperature distribution over the outer and inner surfaces of the radome for five different positions along its axis [22]. This temperature distribution involves a higher temperature at the tip ((T_{out}, T_{in}): (1600°F, 1000°F)) and a relatively lower temperature at the base ((T_{out}, T_{in}): (250°F, 100°F)) of the streamlined radome. The temperature distribution on the radome wall corresponding to any given position on the radome axis is computed using interpolation. Also, the radome wall has a temperature gradient across its thickness.

TABLE 1. Temperature profile of the radome wall: The inner (T_{in}) and outer (T_{out}) temperatures are computed along the radome axis from the base (0.0) to the tip (1.0).

Position on radome axis (m)	Inner Temperature T_{in} (°F)	Outer Temperature T_{out} (°F)
0.00	100	250
0.45	200	575
0.75	300	900
0.95	900	1500
1.00	1000	1600

To optimize the performance of the proposed radomes at hypersonic velocities, the effect of temperature distribution on the radome surface needs to be considered at the design stage. This is accomplished by using inhomogeneous planar layer (IPL) model [23]. In this model, the radome wall is composed of n layers having the same thickness but different dielectric properties to account for the temperature gradient spanning the radome shell thickness. The variation in dielectric properties (ϵ_r, $\tan\delta$) of the radome shell material (Pyroceram 9606) with temperature (°F) is shown in Fig. 3 [24]. The temperature gradient is considered linear, with the innermost layer of the radome shell experiencing the lowest temperature and the outermost layer experiencing the highest temperature. Additionally, the smooth temperature variation from the radome tip to the radome base is also accounted for by the IPL model. However, it is important to note that IPL model is used solely for designing the radome shell, while both the outer ablative layer and inner layer are treated as homogeneous.

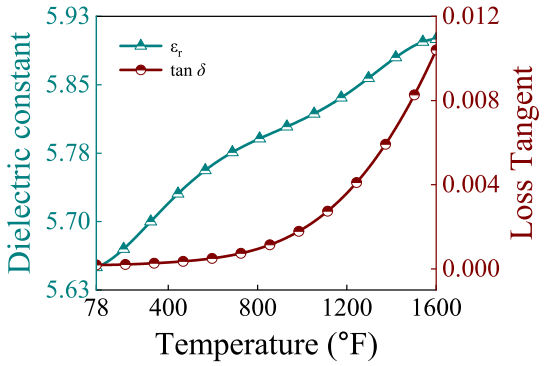

FIGURE 3. Polynomials showing the variation of dielectric properties (ϵ_r, $\tan\delta$) of the radome shell material (Pyroceram 9606) with temperature (°F).

2.4. Computational Technique Used

The PT and BSE characteristics of the antenna-radome system are computed using the MATLAB-based 3-D ray tracing algorithm with aperture integration developed in-house [24, 25].

The outline of this method is as follows. The tangent-ogive radome geometry is defined as [26],

$$r = \sqrt{R^2 - x^2} - B, \tag{1}$$

$$R = \frac{D^2 + 4L^2}{4D}, \tag{2}$$

$$B = R - \frac{D}{2}. \tag{3}$$

Here, L is the length of the radome, and D is the base diameter as shown in Fig. 1. x varies from 0 to L, and r is the radius of the radome at a given x.

The first step in this method is transforming the antenna source points to the radome coordinate system [27]. This is accomplished as follows.

$$[C_{\text{radome}}]_{3\times1} = [R_{\text{EL}}]_{3\times3}[R_{\text{AZ}}]_{3\times3}[C_{\text{Ant}}]_{3\times1} + [X_{\text{g}}]_{3\times1} \tag{4}$$

where $[C_{\text{radome}}]$ and $[C_{\text{Ant}}]$ are coordinates in the radome (x, y, z) and the antenna (x', y', z') coordinate systems, respectively (Fig. 1). $[R_{\text{EL}}]$ and $[R_{\text{AZ}}]$ are the rotation matrices for the rotation of the antenna aperture. z' and y' are the axes of antenna rotation in the elevation (EL) and azimuth (AZ) directions, respectively. $[X_{\text{g}}]$ is the antenna aperture location with respect to the base of the radome.

Following this, the electric field vector and ray vector are defined at each source point on the antenna aperture. Then, the intersection point of the rays on the radome wall (x_o, y_o, z_o) is computed using bi-section method. Thereafter, the angle between the surface normal vector and incident ray vector is calculated at these points. The plane containing both these vectors is referred to as the plane of incidence.

The surface normal vector $\vec{n}$ is given by [28],

$$\vec{n} = n_x\hat{x} + n_y\hat{y} + n_z\hat{z}. \tag{5}$$

For the tangent-ogive geometry, the components of $\vec{n}$ are given by,

$$n_x = \frac{1}{P}, \tag{6}$$

$$n_y = \frac{Q}{P}\frac{y_o}{r_o}, \tag{7}$$

$$n_z = \frac{Q}{P}\frac{z_o}{r_o}. \tag{8}$$

Here,

$$P = \sqrt{1+Q^2}, \tag{9}$$

$$Q = \frac{r_o + B}{x_o}, \tag{10}$$

$$r_o = \sqrt{x_o^2 + y_o^2}. \tag{11}$$

If the incident ray vector is $\vec{k} = k_x\hat{x} + k_y\hat{y} + k_z\hat{z}$, then the angle of incidence θ is obtained as,

$$\theta = \cos^{-1}(\vec{k}\cdot\vec{n}). \tag{12}$$

The transmission coefficient contributed by the radome wall is computed for the parallel and the perpendicular components of the incident ray [29]. To find these components, the perpendicular vector $\vec{D}$ and parallel vector $\vec{G}$ are calculated using the ray vector $\vec{k}$ and surface normal vector $\vec{n}$ as [30],

$$\vec{D} = \vec{n}\times\vec{k}, \tag{13}$$

$$\vec{G} = \vec{D}\times\vec{k}. \tag{14}$$

The perpendicular and parallel components of the incident field are obtained by computing the dot product of $\vec{D}$ and $\vec{G}$ with the incident electric field vector [31], respectively, as

$$E_{\perp}^{i} = \vec{E}^{i}\cdot\vec{D}, \tag{15}$$

$$E_{\parallel}^{i} = \vec{E}^{i}\cdot\vec{G}. \tag{16}$$

By multiplying the respective components of the incident field with that of the complex transmission coefficient, the complex transmitted electric field components are computed as [32],

$$E_{\perp}^{t} = E_{\perp}^{i}T_{\perp}, \tag{17}$$

$$E_{|}^{t} = E_{|}^{i}T_{\parallel}. \tag{18}$$

These components are then recomposed to get the total transmitted electric field and effective complex transmission coefficient.

The complex transmission coefficient T_{mn} of the radome wall is determined for each ray using the ABCD matrix method [29].

T_{mn} can also be resolved into the perpendicular ($T_{\perp}$) and parallel ($T_{\parallel}$) components [33], respectively, as,

$$T_{mn} = T_{\parallel}\cos^2\beta + T_{\perp}\sin^2\beta. \tag{19}$$

where T_{mn} is the complex transmission coefficient contributed by the radome wall for the ray associated with the mnth aperture point (x_{mn}, y_{mn}, z_{mn}), and β is the polarization angle within [0° 90°].

The antenna sum pattern is determined next by using the antenna aperture integration equation [34],

$$S(\theta,\phi) = \frac{\sum_{m=1}^{M}\sum_{n=1}^{N} F_{mn}^{a}T_{mn}e^{-jk(x_{mn}k_x + y_{mn}k_y + z_{mn}k_z)}}{\sum_{m=1}^{M}\sum_{n=1}^{N} F_{mn}^{a}}. \tag{20}$$

where F_{mn}^{a} is the uniform aperture field distribution of the antenna.

After calculating the antenna sum pattern, the PT and BSE are obtained as [35],

$$\text{PT} = S_{\max}, \tag{21}$$

$$\text{BSE} = \angle(S_{\max}). \tag{22}$$

where $S_{\max}$ is the maximum value of the antenna sum pattern in dB, and $\angle(S_{\max})$ is the location of the maximum sum pattern with respect to the boresight direction.

3. DESIGN AND ANALYSIS OF ABLATABLE RADOMES

In this section, constant and variable thickness ablatable radomes are designed and analyzed by computing their PT and BSE characteristics.

3.1. Constant Thickness Ablatable Radome (CTR)

The proposed CTR design has a fixed outer ablative layer thickness of 2 mm and a fixed inner layer thickness of 0.2 mm. The choice of the thickness of the outer ablative layer is governed by its significance in protecting the radome shell from extreme heat and, therefore, has to be thicker than the inner layer. The inner layer is only 0.2 mm as its purpose is to act as a matching layer for avoiding reflections.

The thickness of the radome shell is optimized using the 3-D ray tracing technique by repeated calculation of PT in the EL plane for different radome shell thickness values. The optimization uses the IPL model to account for the temperature dis-

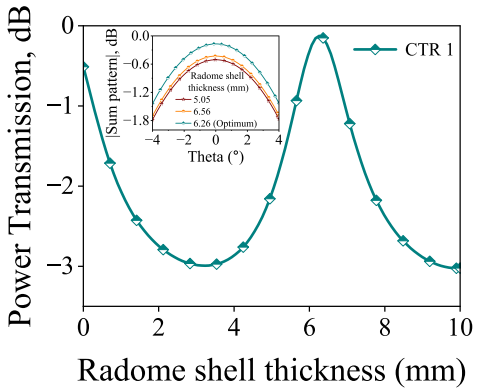

FIGURE 4. Power transmission (dB) as a function of radome shell thickness used to obtain optimum radome shell thickness at antenna scan angle of 3° (for maximum angle of incidence of 68.714°) of CTR 1. The inset shows the magnitude of the main lobe of the antenna sum pattern (dB) for different thicknesses along with the optimum thickness.

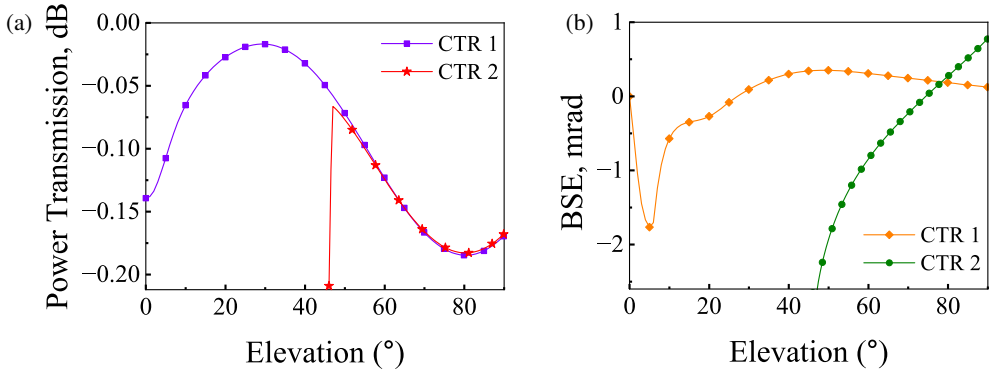

FIGURE 5. (a) Power transmission (dB) and (b) Boresight error (mrad) of CTR 1 and CTR 2 in the EL plane.

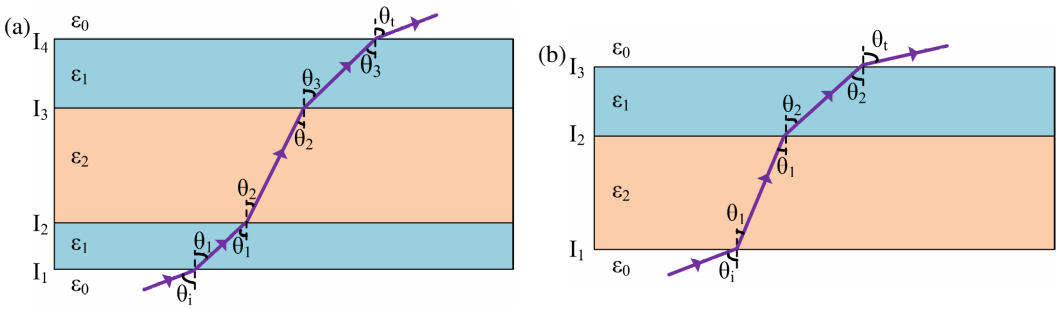

FIGURE 6. Propagation of a ray through radome walls of (a) CTR 1 and (b) CTR 2. The thicknesses of the layers are not to the scale.

tribution in a hypersonic environment. The criterion for thickness optimization is to obtain maximum PT in the EL plane at the highest angle of incidence. For the antenna-radome system of Fig. 1, the calculated maximum angle of incidence of 68.714° is obtained at an antenna scan angle of 3° in the EL plane. Fig. 4 shows the variation of PT with the radome shell thickness at incidence angle of 68.714°. The inset shows the magnitude of the main lobe of the antenna sum pattern (dB) as a function of Theta (θ) in the range $[-4°\ 4°]$ for different radome shell thicknesses. The calculated optimum radome shell thickness at this antenna scan angle is 6.26 mm. Since the same optimum thickness is applied throughout the radome profile, this results in a radome of constant thickness, which will henceforth be referred to as CTR 1 in this paper.

To establish the significance of the inner layer of the wall configuration in ensuring good PT performance, the CTR configuration that does not have the inner layer is also analyzed. This configuration is referred to as CTR 2. The radome wall configuration of CTR 2 has an outer ablative layer with a thickness of 2 mm. The radome shell thickness of CTR 2 was also optimized using the same methodology used for CTR 1. The optimum shell thickness for CTR 2 was found to be 6.3 mm.

The PT and BSE characteristics of both the CTR 1 and CTR 2 in the EL plane are shown in Figs. 5(a) and 5(b), respectively. These and all the subsequent results are computed using the IPL model at temperatures corresponding to a hypersonic environment. From Fig. 5(a), it is evident that CTR 1 provides excellent PT at all antenna scan angles. On the other hand, CTR 2 shows PT only when the antenna scan angle is higher than 46°. From Fig. 5(b), it can be observed that the maximum |BSE| exhibited by CTR 1 is 1.9 mrad. On the other hand, the |BSE| for CTR 2 is higher than that of CTR 1 at most of the antenna scan angles. The BSE of the two configurations is comparable only after 70° scan angle. The PT and BSE performance degradation of CTR 2 is due to the reflection of EM waves at the interface between the radome shell and outer ablative layer. This phenomenon is investigated in more detail in the following.

Figures 6(a) and 6(b) illustrate the propagation of an EM ray through the radome walls of CTR 1 and CTR 2, respectively. Unlike CTR 1, CTR 2 has no inner layer. It consists solely of an outer ablative layer with a dielectric constant lower than the radome shell. As a result, the total internal reflection may occur at the interface I_2 of CTR 2 when the angle of incidence exceeds the critical angle. Such reflections impede the effective propagation of EM waves and might be the reason for the degradation in the performance of CTR 2 for lower antenna scan angles, as observed previously in Fig. 5.

Figure 7 shows the maximum and minimum values of the angle of incidence of incident rays at interface I_2 of CTR 2 in the EL plane. It also shows a horizontal dashed line marking the critical angle of incidence at interface I_2 of CTR 2 wall configuration. It can be observed that at lower antenna scan angles up to 36°, the angle of incidence is always higher than the critical angle. This results in the total internal reflection of rays at I_2. The PT of CTR 2 matches well with that of CTR 1 only when the antenna scan angle is higher than 46°, for which the angle of incidence for all the rays is below the value of the critical angle. Between scan angles of 36° and 46°, the total internal reflection happens for a few rays while other rays pass through the radome wall.

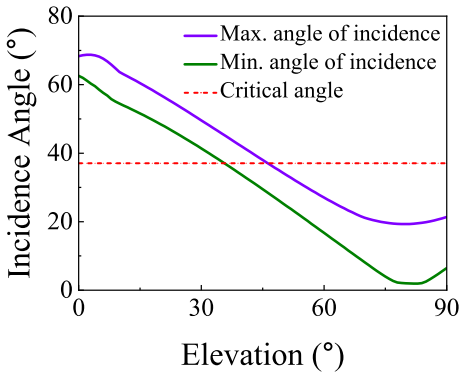

FIGURE 7. Maximum and minimum angles of incidence (°) along with critical angle (°) at the interface (I_2) between the radome shell and the outer ablative layer of CTR 2 in EL plane.

To illustrate this further, the propagation of different rays was observed over the antenna scan angle range of 36° and 46°. This is shown in Fig. 8. It can be seen that at 36°, except for a single ray, all other rays are reflected. At a scan angle of 42°, more rays pass through, although some reflections exist. At 46°, most of the rays are seen to pass through with minimal reflections.

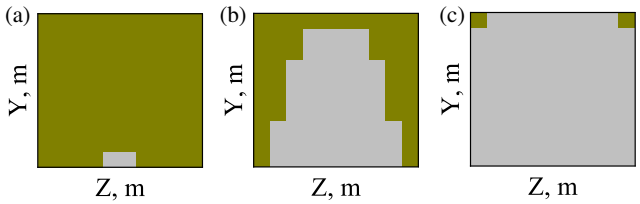

FIGURE 8. Transmission of rays in CTR 2 at antenna scan angles of (a) 36° (b) 42° and (c) 46° in EL plane. Olive indicates areas of no transmission, while grey represents successfully transmitted rays.

The deterioration of the BSE performance of CTR 2 observed in Fig. 5(b) can be further studied by comparing the aperture phase distributions for CTR 1 and CTR 2 as shown in Fig. 9. At 20° scan angle, CTR 2 does not allow the passage of incident rays through the radome. As a result, the aperture phase distribution is zero. On the other hand, changes in the phase over the aperture enclosed by CTR 1 result in non-zero BSE. At 42°, reduction in phase change over antenna aperture results in lower BSE in CTR 1. On the other hand, only some rays find passage through the radome wall of CTR 2. This results in increased phase changes across the antenna aperture, leading to higher BSE in CTR 2. At a scan angle of 70°, the phase distributions of CTR 1 and CTR 2 are similar, resulting in similar BSE performances of both the radomes at higher antenna scan angles. The analysis demonstrates that CTR 1 outperforms CTR 2 in both PT and BSE, justifying the decision to select CTR 1 wall configuration.

3.2. Variable Thickness Ablatable Radome (VTR)

To improve the power transmission of the radome for the entire antenna scan angle range, the design of a variable thickness ablatable radome (VTR) is attempted. For this radome, the thicknesses of the outer ablative layer and inner matching layer are

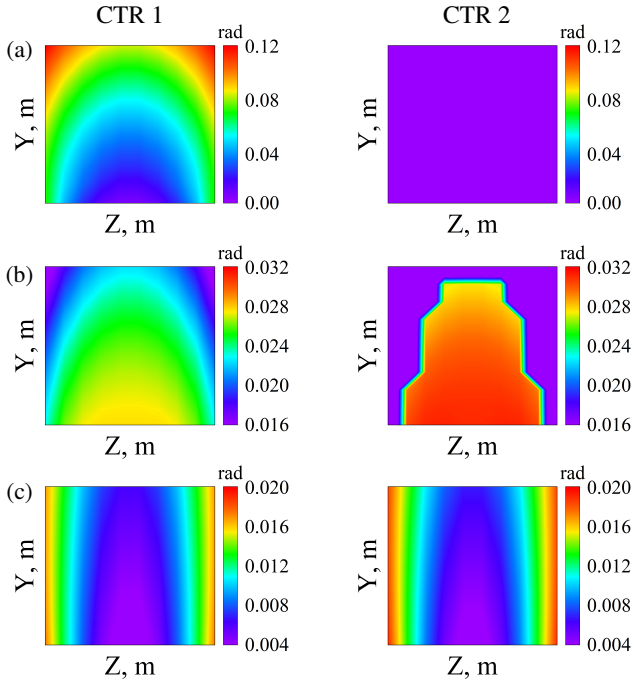

FIGURE 9. Aperture phase distribution of CTR 1 and CTR 2 at antenna scan angles of (a) 20° (b) 42° and (c) 70° in EL plane.

fixed at 2 mm and 0.2 mm, respectively. The thickness of the radome shell is optimized at each antenna scan angle using the IPL model. Fig. 10 shows PT (dB) as a function of radome shell thickness (mm) computed at different antenna scan angles. It can be observed that the PT reaches a maximum for radome shell thickness between 5.5 mm and 6.5 mm at all antenna scan angles. The optimum radome shell thickness is computed at each antenna scan angle for maximum power transmission. The optimum radome shell thicknesses are tabulated in Table 2. The resulting VTR design has a radome shell thickness of 6.32 mm at the radome tip and 5.93 mm at the radome base. The temperature distribution used in the IPL model for the VTR design is the same as that used for CTR 1. However, the coefficient of thermal expansion (α) of the radome wall due to temperature gradient is also considered in calculating the optimum value of the shell thickness in the VTR design [36]. The values of α for the radome wall materials are referenced from [20] and [21].

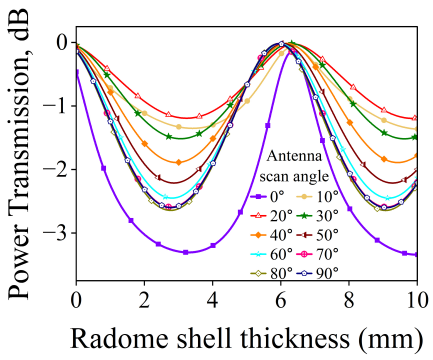

FIGURE 10. Power transmission (dB) as a function of radome shell thickness used to obtain optimum radome shell thickness (mm) at different antenna scan angles (°) of VTR.

TABLE 2. Optimum radome shell thickness (mm) computed at different antenna scan angles (°) with corresponding positions on the radome axis (m) for VTR.

Antenna scan angle (°)	Position on radome axis (m)	Optimum radome shell thickness (mm)
0	1	6.32813
10	0.80939	6.35596
20	0.67993	6.38468
30	0.58887	6.29365
40	0.52073	6.16277
50	0.46631	6.06209
60	0.42012	5.98153
70	0.37862	5.93107
80	0.33928	5.91069
90	0.30040	5.93037

The PT and BSE characteristics of the VTR design are computed and are presented for comparison with that of CTR 1 in Fig. 11(a) and Fig. 11(b), respectively. The analysis shows improved PT performance of VTR compared to CTR 1 (Fig. 11(a)). This enhancement can be attributed to the unique shell thickness computed for each scan angle, which ensures maximum PT performance even at higher antenna scan angles. The superior performance of the VTR at elevated antenna scan angles is further validated by the inset in Fig. 11(a). This inset illustrates the magnitude of the main lobe of the antenna sum pattern for CTR 1 and VTR. It is evident that VTR outperforms CTR 1 at higher antenna scan angles.

The VTR shows a higher BSE than the CTR 1 in both EL and AZ planes (Fig. 11(b)). This is because of significant phase changes induced on the underlying antenna aperture due to the variable thickness nature of the radome [37]. In the literature, many VTR designs that optimize PT are presented. However, optimizing the radome wall profile for simultaneous improvement in PT and BSE requires more sophisticated methods, such as the one presented in [38].

4. PERFORMANCE IN DYNAMIC FLIGHT CONDITIONS

In this section, the performances of both the CTR 1 and VTR are computed over 90 time steps during which the temperature experienced by the radomes changes from the ambient temperature to the hypersonic temperature. This study is essential as it provides a detailed insight into how the performance characteristics of the proposed radomes vary under dynamic flight conditions. At the beginning of this analysis, the entire radome is at ambient temperature. At the final time step, the radome reaches the temperature distribution of the hypersonic environment. The variation in the electrical properties of radome shell material with temperature is referenced from Fig. 3 [24]. Since the outer ablative layer and inner matching layer are homogeneous, their electrical properties are considered constant [21].

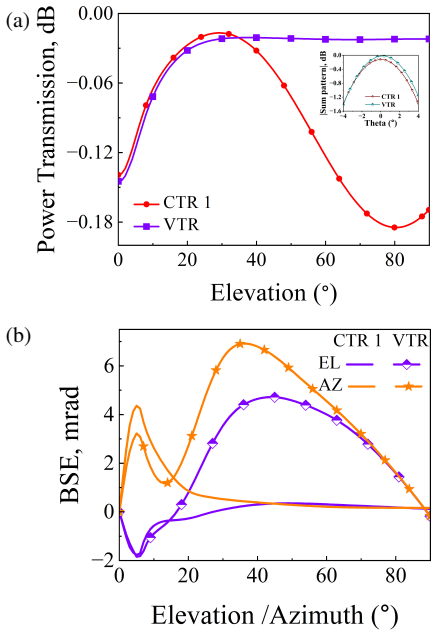

FIGURE 11. (a) Power transmission (dB) in EL plane and (b) Boresight error (mrad) in EL and AZ planes at different antenna scan angles (°) for CTR 1 and VTR. The inset in (a) shows the magnitude of the main lobe of the antenna sum pattern (dB) for CTR 1 and VTR.

4.1. CTR 1

Figures 12(a) and 12(b) present the co-polar (co-pol) and the cross-polar (cross-pol) power transmission characteristics of the CTR 1 in the EL plane, respectively. Except for the scan angle range from 0° to 10° around the ambient temperatures, CTR 1 exhibits excellent co-pol PT (≥ -0.4 dB) for all operating conditions. Also, CTR 1 exhibits slightly higher cross-pol PT (-20 dB) for lower scan angle ranges. However, the cross-pol PT is well below -30 dB for the rest of the operating conditions.

The BSE characteristics of the CTR 1 in both EL and AZ planes under dynamic flight conditions are shown in Figs. 12(c) and 12(d), respectively. The |BSE| in both EL and AZ planes degrade only at lower scan angles (0°–10°) near the ambient temperatures. For all other operating conditions, a good BSE performance (≤ 0.5 mrad) can be observed. The performance degradation at lower antenna scan angles results from an abrupt phase change when the antenna beam encounters the sharp and narrow cross-section of the radome tip, leading to increased transmission loss and boresight error.

4.2. VTR

The dynamic in-flight co-pol and cross-pol PT performances of the VTR in the EL plane are shown in Figs. 13(a) and 13(b), respectively. The PT degrades at lower scan angles (0°–10°) near the ambient temperature. However, the VTR has excellent PT (≥ -0.2 dB) characteristics at mid and higher scan angles, irrespective of the operating conditions.

The |BSE| of the VTR in both EL and AZ planes are shown in Figs. 13(c) and 13(d), respectively. The |BSE| in the EL plane degrades around 5° scan angle near the ambient tempera-

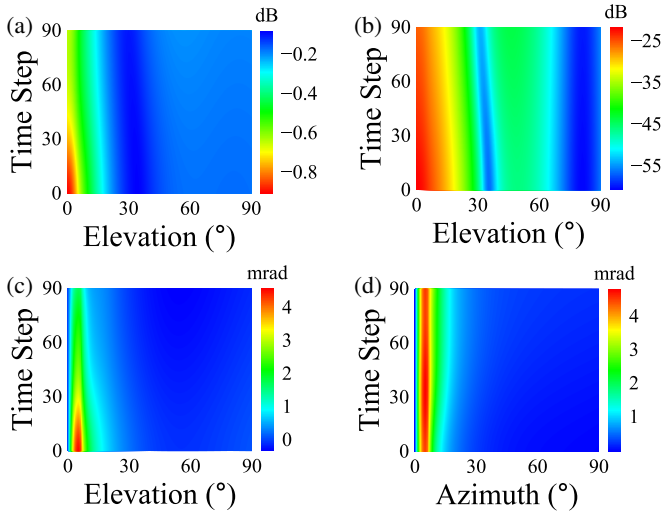

FIGURE 12. (a) Co-polar PT (dB), and (b) Cross-polar PT (dB) in EL plane. |BSE| (mrad) in (c) EL plane, and (d) AZ plane of CTR 1.

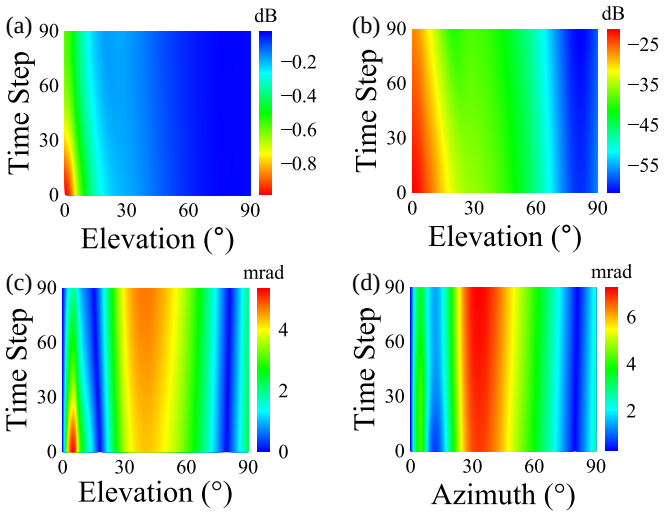

FIGURE 13. (a) Co-polar PT (dB), and (b) Cross-polar PT (dB) in EL plane. |BSE| (mrad) in (c) EL plane, and (d) AZ plane of VTR.

ture. However, it improves when the operating temperature increases. In the mid-scan angle range, the |BSE| reaches a peak of 4 mrad but is seen to improve significantly at higher scan angles. The |BSE| in the AZ plane becomes minimum around 10° and 80°, and it remains high at other scan angles.

Interestingly, for scan angles greater than 10°, the CTR 1 and VTR performance characteristics are not significantly affected by the operating conditions but rather by the operating scan angle, resulting in a stable performance. This is expected since the electrical properties of the materials chosen are stable with respect to temperature. This advantage makes these radomes good candidates for high-velocity applications.

5. EFFECT OF ABLATION

In this section, the performances of the CTR 1 and VTR during the ablation of the outer ablative layer are computed. The ablation profile considered is uniform over the entire radome surface. Due to the lack of practical nonuniform ablation data, the ablation profile considered here is not associated with any specific trajectory of airborne vehicles in the hypersonic environment. The analysis considers reduction in the outer ablative layer from 2 mm to 0 mm in the steps of 0.5 mm. The IPL model with the temperature distribution of the hypersonic environment is used to compute the performance parameters.

5.1. CTR 1

The PT characteristics of the CTR 1 during ablation are shown in Fig. 14(a). As the thickness of the outer ablative layer decreases, the PT performance degrades when the antenna scan angle is between 0° and 40°. However, the PT is seen to improve for higher scan angles $> 40°$. Moreover, the overall PT of the radome is well above -0.6 dB post-ablation.

The effects of ablation on the BSE characteristics of CTR 1 in EL and AZ planes are shown in Figs. 14(b) and 14(c), respectively. In the EL plane, a significant increase in |BSE| is observed for lower scan angles (0° to 15°). However, |BSE| remains unaffected by ablation for the rest of the operating scan angle range. In the AZ plane, the |BSE| is affected by ablation in the lower and mid-scan angle ranges (0° to 45°). Furthermore, the peak value of |BSE| observed in the AZ plane is higher than that in the EL plane.

5.2. VTR

The PT characteristics of the VTR computed during ablation are shown in Fig. 15(a). With the decrease in outer ablative layer thickness, a corresponding degradation in PT performance can be observed, with PT reaching a minimum value when the outer ablative layer completely vanishes. However, the overall PT of VTR is above -0.5 dB throughout the operating scan angle range, even in the absence of the outer ablative layer.

The changes in the BSE characteristics of VTR show similar trends to those observed for CTR 1, as shown in Figs. 15(b) and 15(c). In the EL plane, degradation is observed only at lower scan angles, and the BSE remains unchanged for the rest of the scan angle range. In the AZ plane, BSE degrades for both lower and mid-scan angle ranges. Additionally, the |BSE| value is higher in the AZ plane than that in the EL plane.

It is worth noting that the overall PT and BSE performance of VTR is superior to that of CTR 1 during ablation. It can also be concluded that the proposed radomes produce a relatively stable BSE regardless of the change in ablative layer thickness for all scan angles greater than 20°.

6. PERFORMANCE OVER BROADBAND

Although the antenna-radome system considered in this work is designed to operate at 10 GHz, it is well known that the multilayer radomes have the ability to provide broadband performance. To explore this quality of multi-layer radomes, the performances of CTR 1 and VTR are computed across the X-band from 8 GHz to 12 GHz. For this computation, the spacing between the source points of 10×10 antenna array is 0.5λ, where λ is now the wavelength corresponding to the frequency of 12 GHz. The performance was computed using the IPL model for the temperature distribution of the hypersonic

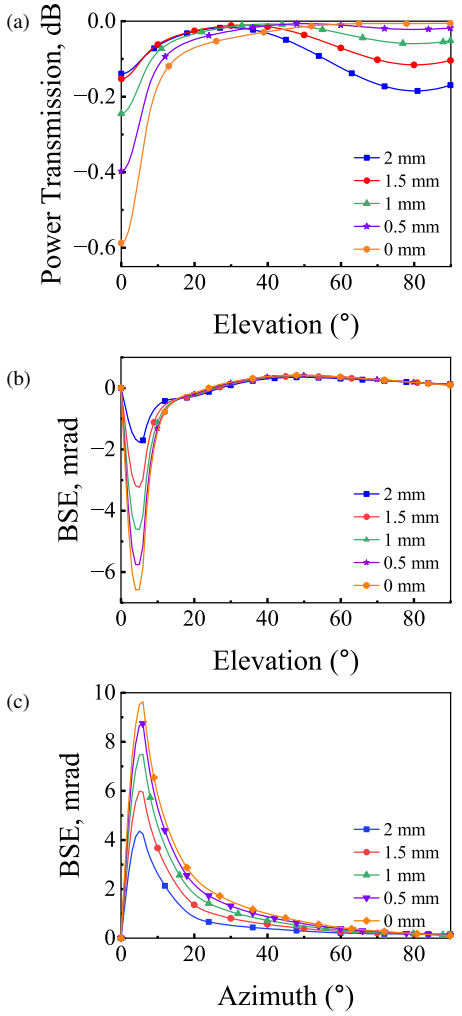

FIGURE 14. (a) Power transmission (dB) in EL plane and Boresight error (mrad) in (b) EL and (c) AZ planes with antenna scan angles (°) for different ablative layer thicknesses (mm) in CTR 1.

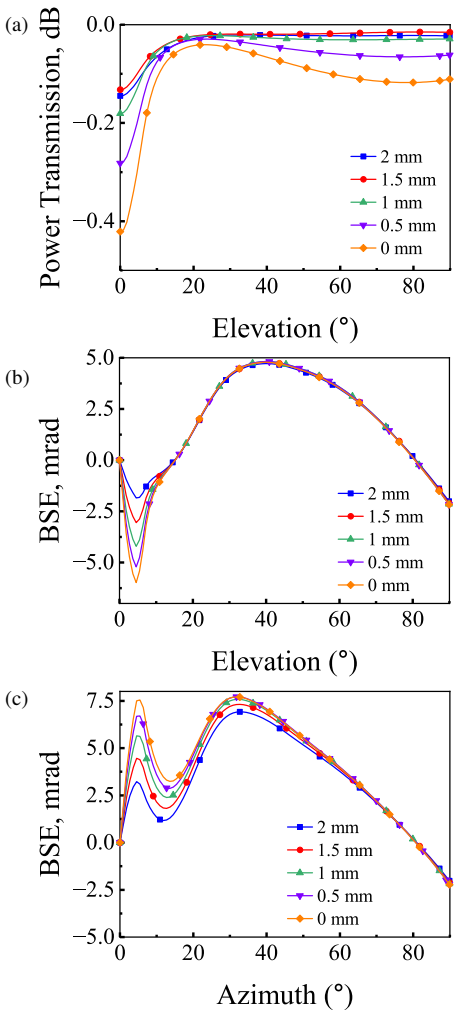

FIGURE 15. (a) Power transmission (dB) in EL plane and Boresight error (mrad) in (b) EL and (c) AZ planes with antenna scan angles (°) for different ablative layer thicknesses (mm) in VTR.

environment. First, it was verified that the performance of the proposed radomes did not change due to the change in the spacing between the source points. Then, the performance of both CTR 1 and VTR was analyzed over the X-band at different antenna scan angles.

Figure 16(a) shows the variation in PT with frequency for both CTR 1 and VTR at different antenna scan angles over the X-band having a full ablative layer thickness of 2 mm. When the antenna scan angle is 0°, both the radomes provide a relatively narrow band PT performance. At 15°, both the radomes provide PT higher than −1 dB over the entire band. As the antenna scan angle increases, the PT decreases at the frequencies away from the center frequency. From 0° to 30°, the PT performances of CTR 1 and VTR are similar. However, at 60° scan angle, the peak of PT for CTR 1 is shifted towards lower frequencies. As a result, the PT of CTR 1 is higher than that of VTR at lower frequencies. On the other hand, VTR performs better than CTR 1 for higher frequencies at 60° scan angle.

The PT performances of the CTR 1 and VTR over the X-band frequency are also analyzed by calculating the −0.5 dB power transmission bandwidth (%) for different thicknesses of the outer ablative layer. This is tabulated in Table 3. As expected, the bandwidths are the lowest at 0° and highest at 15° antenna scan angles, respectively. The bandwidth of VTR is observed to be higher than CTR 1 for all antenna scan angles. Also, it should be noted that the bandwidths remain reasonably stable with the reduction in the thickness of the outer ablative layer.

Figure 16(b) shows the variation in BSE with frequency for both the CTR 1 and VTR at different antenna scan angles having a full ablative layer thickness of 2 mm. Due to the symmetry of the radome seen by the enclosed antenna, both the radomes produce no BSE at 0° scan angle. At a scan angle of 15°, the two radomes exhibit similar BSE with the maximum of 3 mrad in |BSE|. However, at scan angles of 30° and 60°, VTR exhibits higher BSE than CTR 1. The maximum variation in |BSE| for CTR 1 is 1.49 mrad and 0.38 mrad at 30° and 60° scan angles, respectively. The maximum variation in |BSE| for VTR is 4.26 mrad and 3.62 mrad at 30° and 60° scan angles, respectively.

TABLE 3. −0.5 dB PT bandwidth (%) of CTR 1 and VTR at different antenna scan angles (°) and ablative layer thicknesses (mm).

Ablative Layer Thickness (mm)	Antenna Scan Angle (°)							
	0°		15°		30°		60°	
	CTR 1	VTR	CTR 1	VTR	CTR 1	VTR	CTR 1	VTR
2.0	7.07	7.79	39.92	44.72	30.54	34.84	20.98	25.36
1.5	7.70	8.68	39.96	45.03	30.04	34.30	20.82	25.07
1.0	8.12	9.19	40.02	45.29	29.74	33.98	20.67	24.82
0.5	8.41	9.53	40.14	45.51	29.68	33.91	20.65	24.75
0.0	8.58	9.73	40.31	45.70	30.98	35.42	20.85	24.95

TABLE 4. The performance of the proposed radomes compared to the existing literature.

Reference	No. of Layers	Antenna type	Maximum Co-polar PT (dB)	Maximum Cross-polar PT (dB)	Total PT (dB)	$\|BSE\|_{max}$ in EL plane (mrad)
Constant Thickness Radomes						
[24]	1	Aperture array	−0.12	−33.4	-	1.8
[39]	7	Monopulse array	−0.18	below −30	-	2.5
[40]	7	Slotted waveguide	−0.18	−20	-	2.6
[41]	1	Slotted waveguide	−0.18	−37	-	5
[42]	3	Slotted waveguide	−0.50	−25	-	3.8
Our work	3	Aperture array	−0.10	−25.82	−0.01	1.76
Variable Thickness Radomes						
[37]	1	Aperture array	−0.20	−35	−0.006	2.4
[38]	1	Monopulse planar array	–	-	−0.6	5
[40]	7	Slotted waveguide	−0.18	−20	-	2.6
[43]	1	Circular aperture	-	-	−0.3	3
[44]	9	Slotted waveguide	−0.76	-	-	0.5
Our Work	3	Aperture array	−0.029	−27.01	−0.02	4.71

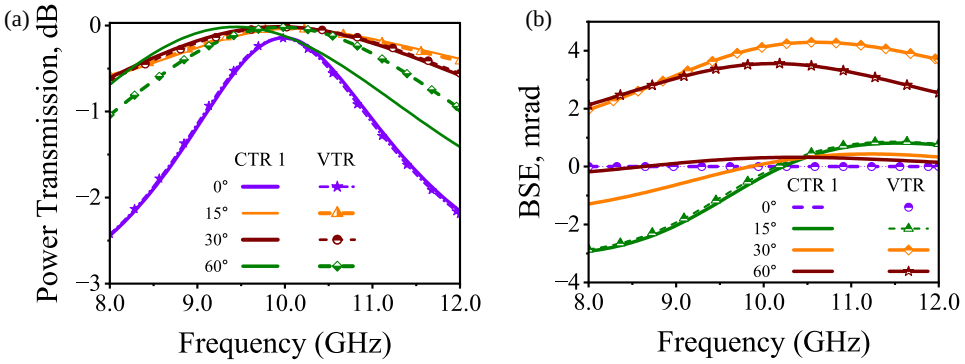

FIGURE 16. (a) Power transmission (dB) and (b) Boresight error (mrad) of CTR 1 and VTR in the EL plane at different antenna scan angles (°) over the X-band having a full ablative layer thickness of 2 mm.

7. PERFORMANCE COMPARISON

The performance of the proposed radome designs is compared with those available in the existing literature, as presented in Table 4. The performance parameters of our CTR 1 and VTR designs correspond to a radome configuration with the full thickness of the outer ablative layer and were analyzed using the IPL model at the hypersonic temperature distribution. The antenna-radome systems chosen for the comparison use different X-band antennas, as shown, but they all use tangent-ogive geometry for the radomes. Except [38] and [42], all the other radomes are analyzed using the IPL model. The literature presents PT performance as a total PT or as separate co-pol and cross-pol

PT. Therefore, Table 4 has both these columns to allow appropriate comparison.

Compared to the CTR designs in [24, 39–42], the proposed CTR 1 design has the highest co-pol PT. The cross-pol PT of CTR 1 is comparable to [42] and better than [40]. Also, the proposed CTR 1 design has the lowest $|\mathrm{BSE}|_{\max}$ in the elevation plane among the designs chosen for comparison. The proposed VTR design has a better co-pol or total PT than other VTRs. The $|\mathrm{BSE}|_{\max}$ of VTR in the EL plane is lower than that of [38] while it is higher than that of the other radomes.

8. CONCLUSION

This paper presents two streamlined radome designs: constant thickness ablatable radome (CTR 1) and variable thickness ablatable radome (VTR) for hypersonic applications. The comprehensive analysis of ray propagation through the radome wall and the aperture phase distribution study demonstrates the effectiveness of the selected radome wall configuration by showing improvements in PT and BSE. The thickness of the radome shells has been optimized for both designs. Numerical results obtained using the 3-D ray tracing method with aperture integration indicate that the proposed radomes maintain stable performance over the designed thermal operating range of 250°F to 1600°F. During the dynamic flight operation, the co-pol PT for CTR 1 and VTR is found to be -0.1 dB and -0.029 dB, respectively. Even after complete ablation, the power transmission of CTR 1 and VTR remains well above -0.6 dB and -0.5 dB, respectively. The maximum BSE for CTR 1 and VTR is found to be 1.76 mrad and 4.71 mrad, respectively. Both radome designs demonstrate optimal performance over the X-band, providing reasonably stable PT and BSE across a broad frequency range. These features make them suitable for hypersonic airborne applications, regardless of temperature effects and material ablation.

Now, we present some limitations and challenges pertaining to the design of streamlined ablatable radomes for hypersonic applications.

- Conducting experiments on an antenna enclosed by a streamlined radome presents significant complexities, including the high cost of radome fabrication and the requirement for sophisticated infrastructure.
- Optimizing VTR for minimum BSE at all antenna scan angles requires global and simultaneous optimization of wall thicknesses for the VTR profile. This requires more advanced methodology such as MOPSO (Multiobjective particle swarm optimization), and it usually results in a complex wall thickness profile.
- Designing radomes for hypersonic applications requires materials that can withstand extreme thermal and mechanical stresses while maintaining electromagnetic transparency. Such materials can be very costly and require complex and time-consuming manufacturing processes. Also, temperature-dependent material data for the design and optimization of radomes for hypersonic applications is very limited.
- At high velocities, as the outer layer of the radome ablates, a thin layer of plasma might form on the radome surface. The properties of this plasma layer depend on temperature, pressure, and chemical reactions happening near the radome surface. Due to these multiple factors, it is difficult to predict the realistic properties of the plasma layer.

Future research could focus on improving the BSE for VTR design and analyzing radomes covered by plasma sheaths in a hypersonic environment.

ACKNOWLEDGEMENT

This work was supported by the Aeronautics Research and Development Board of Defence Research and Development Organization, Government of India. We are thankful to Shri. G. V Ramakoteshwar Rao for valuable discussions during the preparation of this manuscript.

REFERENCES

[1] Dan, Y. and J. Yang, "Electromagnetic performance analysis of inhomogeneous radome walls considering temperature and ablation," *Aerospace*, Vol. 10, No. 11, 927, 2023.

[2] Zhou, L., Y. Pei, R. Zhang, and D. Fang, "Design for broadband high-temperature radome wall with graded porous structure," *AIAA Journal*, Vol. 50, No. 9, 1956–1963, 2012.

[3] Weckesser, L. B., R. K. Frazer, D. J. Yost, B. E. Kuehne, G. P. Tricoles, R. Hayward, and E. L. Rope, "Aerodynamic heating effects on radome boresight errors," in *Proceeding of 14th Symposium on Electromagnetic Windows*, 45–51, Atlanta, GA, USA, 1978.

[4] Kozlovskiy, V., V. Kozlovskiy, O. Nimych, L. Klobukova, and N. Yakymchuk, "Model of the flat fairing antenna dielectric layer with aerodynamic heating," *Informatyka, Automatyka, Pomiary w Gospodarce I Ochronie Środowiska*, Vol. 13, No. 4, 119–125, 2023.

[5] Favaloro, M., "Ablative materials," in *Kirk-Othmer Encyclopedia of Chemical Technology*, John Wiley & Sons, Inc., 2000.

[6] Brey, H., "Performance evaluation for a class of asymetrically ablated duroid radomes," in *15th Symposium on Electromagnetic Windows*, 117–127, 1980.

[7] Mehmedagic, I. and S. Thangam, "Modeling and simulation of aerodynamic nosecone ablation," in *Heat Transfer Summer Conference*, Vol. 87905, V001T12A001, American Society of Mechanical Engineers, 2024.

[8] Denis, F., R. Hruschka, M. Bastide, B. Sauerwein, Y. Hoarau, and R. Mose, "Experimental investigation of thermal ablation by melting in a hypersonic shock tunnel," *Journal of Spacecraft and Rockets*, Vol. 59, No. 4, 1406–1411, 2022.

[9] Amar, A. J., B. Oliver, B. Kirk, G. Salazar, and J. Droba, "Overview of the charring ablator response (char) code," in *46th AIAA Thermophysics Conference*, 3385, Washington, D.C., 2016.

[10] Seo, M.-G. and M.-J. Tahk, "Observability analysis and enhancement of radome aberration estimation with line-of-sight angle-only measurement," *IEEE Transactions on Aerospace and Electronic Systems*, Vol. 51, No. 4, 3321–3331, 2015.

[11] Wang, C., Y. Wang, Y. Chen, W. Gao, Q. Xu, Z. Wang, J. Liu, C. Zhou, W. Xu, and J. Zhong, "Coupling model and electronic compensation of antenna-radome system for hypersonic vehicle

with effect of high-temperature ablation," *IEEE Transactions on Antennas and Propagation*, Vol. 68, No. 3, 2340–2355, 2019.

[12] He, X.-Y., D.-H. Kong, W.-W. Zhang, and M.-Y. Xia, "An efficient volume integral equation method for analysis of boresight error of a radome with minor ablation," *Electronics*, Vol. 11, No. 23, 3861, 2022.

[13] Duan, W., X. Weng, Y. Li, Z. Li, S. Bao, and M. Bi, "Temperature-dependent electromagnetic performance predictions of a hypersonic radome based on variable thickness gradient dielectric multilayer walls," *IEEE Antennas and Wireless Propagation Letters*, Vol. 23, No. 8, 2381–2385, 2024.

[14] Duan, W., J. Xie, M. Bi, L. Qi, Y. Li, K. Li, Z. Li, and X. Weng, "Study on the electromagnetic performance of radome with laminar ablation for reentry applications," *IEEE Transactions on Antennas and Propagation*, Vol. 72, No. 8, 6261–6269, 2024.

[15] Kozakoff, D. J. and A. Ossin, "Design of an ablative missile radome for use with a shaped beam antenna," *Electromagnetic Windows*, 29, 1978.

[16] Epperson, E. H., Jr., "Adaptively ablatable radome," US Patent 5,457,471, Oct. 1995.

[17] Sonalikar, H. S., "Temperature dependent EM investigation of inhomogeneous dielectric wall for application in ablatable radome," in *2018 IEEE Indian Conference on Antennas and Propogation (InCAP)*, 1–5, Hyderabad, India, 2018.

[18] Aparna, A. P. and H. S. Sonalikar, "Temperature dependent electromagnetic design of dielectric wall for airborne applications," in *2019 IEEE Indian Conference on Antennas and Propogation (InCAP)*, 1–5, Ahmedabad, India, 2019.

[19] Barik, R. N., A. P. Aparna, and H. S. Sonalikar, "Electromagnetic design of planar ablatable radome using inhomogeneous planar layer model," in *2023 IEEE Microwaves, Antennas, and Propagation Conference (MAPCON)*, 1–5, Ahmedabad, India, 2023.

[20] Crone, G. A. E., A. W. Rudge, and G. N. Taylor, "Design and performance of airborne radomes: A review," in *IEE Proceedings F (Communications, Radar and Signal Processing)*, Vol. 128, No. 7, 451–464, 1981.

[21] Ehrlich, P., L. E. Amborski, and R. L. Burton, "Dielectric properties of teflon from room temperature to 314 C and from frequencies of 102 to 105 c/s," *Journal of Research of the National Bureau of Standards*, Vol. 51, 185–188, 1953.

[22] Kilcoyne, N. R., "A two-dimensional ray-tracing method for the calculation of radome boresight error and antenna pattern distortion," 2767–2, Defense Technical Information Center, FJlectro Science Lab., Ohio State Univ. Res. Foundation Rep., 1969.

[23] Nair, P. R. U. and R. M. Jha, "Temperature dependent EM performance predictions of dielectric slab based on inhomogeneous planar layer model," in *Proceedings of the 2012 IEEE International Symposium on Antennas and Propagation*, 1–2, Chicago, IL, USA, 2012.

[24] Parameswaran, A. and H. S. Sonalikar, "Design of airborne radome using novel temperature dependent electromagnetic modeling," *Progress In Electromagnetics Research C*, Vol. 104, 37–52, 2020.

[25] Gao, X. and L. Felsen, "Complex ray analysis of beam transmission through two-dimensional radomes," *IEEE Transactions on Antennas and Propagation*, Vol. 33, No. 9, 963–975, 1985.

[26] Nair, R. U. and R. M. Jha, "Electromagnetic performance analysis of a novel monolithic radome for airborne applications," *IEEE Transactions on Antennas and Propagation*, Vol. 57, No. 11, 3664–3668, 2009.

[27] Shavit, R., *Radome Electromagnetic Theory and Design*, John Wiley & Sons, 2018.

[28] Kozakoff, D. J., *Analysis of Radome-Enclosed Antennas*, 2nd ed., Artech House, 2010.

[29] Volakis, J. L., *Antenna Engineering Handbook*, Mcgraw-Hill New York, 2007.

[30] Shin, H., D. Yoon, D.-Y. Na, and Y. B. Park, "Analysis of radome cross section of an aircraft equipped with a FSS radome," *IEEE Access*, Vol. 10, 33 704–33 712, 2022.

[31] Tricoles, G. P., "Radome electromagnetic design," in *Antenna Handbook: Theory, Applications, and Design*, 2051–2081, Springer, 1988.

[32] Wang, B., M. He, J. Liu, H. Chen, G. Zhao, and C. Zhang, "An efficient integral equation/modified surface integration method for analysis of antenna-radome structures in receiving mode," *IEEE Transactions on Antennas and Propagation*, Vol. 62, No. 9, 4884–4889, 2014.

[33] Xu, W., B. Y. Duan, P. Li, and Y. Qiu, "Study on the electromagnetic performance of inhomogeneous radomes for airborne applications — Part I: Characteristics of phase distortion and boresight error," *IEEE Transactions on Antennas and Propagation*, Vol. 65, No. 6, 3162–3174, 2017.

[34] Nair, R. U. and R. M. Jha, "Electromagnetic design and performance analysis of airborne radomes: Trends and perspectives [antenna applications corner]," *IEEE Antennas and Propagation Magazine*, Vol. 56, No. 4, 276–298, 2014.

[35] Yang, L., Y. Li, Q. Chen, D. Zhang, Q. Fei, and J. Liu, "Electromagnetic design method of radomes under high temperature environment," *IEEE Transactions on Antennas and Propagation*, 1–1, 2025.

[36] Ho, C. Y. and R. E. Taylor, *Thermal Expansion of Solids*, ASM International, 1998.

[37] Parameswaran, A., H. S. Sonalikar, and D. Kundu, "Temperature-dependent electromagnetic design of inhomogeneous planar layer variable thickness radome for power transmission enhancement," *IEEE Antennas and Wireless Propagation Letters*, Vol. 20, No. 8, 1572–1576, 2021.

[38] Xu, W., B. Y. Duan, P. Li, N. Hu, and Y. Qiu, "Multiobjective particle swarm optimization of boresight error and transmission loss for airborne radomes," *IEEE Transactions on Antennas and Propagation*, Vol. 62, No. 11, 5880–5885, 2014.

[39] Nair, R. U., M. Suprava, and R. M. Jha, "Graded dielectric inhomogeneous streamlined radome for airborne applications," *Electronics Letters*, Vol. 51, No. 11, 862–863, 2015.

[40] Yazeen, P. S. M., C. V. Vinisha, S. Vandana, M. Suprava, and R. U. Nair, "Electromagnetic performance analysis of graded dielectric inhomogeneous streamlined airborne radome," *IEEE Transactions on Antennas and Propagation*, Vol. 65, No. 5, 2718–2723, 2017.

[41] Nair, R., S. Vandana, S. Sandhya, and R. M. Jha, "Temperature-dependent electromagnetic performance predictions of a hypersonic streamlined radome," *Progress In Electromagnetics Research*, Vol. 154, 65–78, 2015.

[42] Zhou, L., Y. Pei, and D. Fang, "Dual-band a-sandwich radome design for airborne applications," *IEEE Antennas and Wireless Propagation Letters*, Vol. 15, 218–221, 2015.

[43] Xu, W., B. Y. Duan, P. Li, and Y. Qiu, "Study on the electromagnetic performance of inhomogeneous radomes for airborne applications — Part II: The overall comparison with variable thickness radomes," *IEEE Transactions on Antennas and Propagation*, Vol. 65, No. 6, 3175–3183, 2017.

[44] Wang, Z., L. Tang, L. Zhou, Z. Jiang, Z. Liu, and Y. Liu, "Methodology to design variable-thickness streamlined radomes with graded dielectric multilayered wall," *IEEE Transactions on Antennas and Propagation*, Vol. 69, No. 11, 8015–8020, 2021.